



## Supporting Information

### **Anion Storage Chemistry of Organic Cathodes for High-Energy and High-Power Density Divalent Metal Batteries**

*Y. Xiu, A. Mauri, S. Dinda, Y. Pramudya, Z. Ding, T. Diemant, A. Sarkar, L. Wang, Z. Li, W. Wenzel, M. Fichtner, Z. Zhao-Karger\**

## SUPPORTING INFORMATION

## Experimental

**Synthesis of PTPAn:** PTPAn was prepared according to a previously reported procedure.<sup>[1]</sup> Typically, triphenylamine (TPA, 6.133 g, 25 mmol) was first dissolved in 100 ml chloroform (CHCl<sub>3</sub>). FeCl<sub>3</sub> (4.055 g, 25 mmol) was then added to the solution in four portions with an interval of 1 h. Subsequently, the mixture was kept at room temperature for 4 h for polymerization. Then it was poured into 150 ml methanol. The yellow product precipitated immediately and was filtered. Then it was washed with methanol for 3 times. Finally, it was purified by re-precipitation from solution of chloroform and acetone with 5% of aqueous ammonia. In order to remove the short chain soluble, the polymer was further purified by Soxhlet extraction in 1, 2-dimethoxyethane (DME) for 48 h and dried at 85 °C for 12 h under vacuum.

**Materials preparation:** The electrolyte salt of magnesium tetrakis(hexafluoroisopropoxy) borate was synthesized following our previous report.<sup>[2]</sup> The PTGNP composite was prepared by dissolving the as-synthesized PTPAn in chloroform and mixed with graphene nanoplates in a mass ratio of 1: 1. After stirring under argon for 24 h, the suspension was further treated by ultrasonic homogenization. The mixture was then dried under vacuum. The PTPAn@GNP composite was obtained after ball-milling at 200 rpm for 2 h.

**Materials characterization:** The PTPAn was characterized by nuclear magnetic resonance spectroscopy (NMR, Bruker Advance II 500 spectrometer) using CDCl<sub>3</sub> as solvent and Fourier-transform infrared spectroscopy (FT-IR, Spectrum Two, PERKIN ELMER). The morphology of the PTGNP composite and the electrodes was characterized by SEM (ZEISS LEO 1530, at 15 kV) and TEM (ThermoFisher Scientific Themis 300, at 300 kV).

**Operando Raman spectroscopy** was utilized to deduce the oxidation and reduction mechanism of the PTPAn cathode material during the discharge and charge processes. The spectra were collected at room temperature in the spectral range 700-1800 cm<sup>-1</sup> by using an inVia™ confocal Raman microscope (RENISHAW) with a 532 nm excitation laser. The nominal laser power was filtered down to ~2.5 mW to avoid sample overheating. The slit opening of the confocal system was fixed at 65 μm and centered at 1867 μm. The spectra were collected in backscattering geometry with a 50X objective (confocal micro-Raman mode). To increase the signal-to-noise ratio, each spectrum was recorded with 40 s acquisition time. During the charge/discharge cycle, Raman spectra were collected in an 1 min interval. *Operando* Raman measurements were carried out using an ECC-Opto-Std (EL-CELL® GmbH) electrochemical cell connected with Raman microscope. The *in situ* cell was assembled using a PTGNP cathode and Mg metal as an anode. The cathode side of the cell was sealed with a thin optical glass window (0.15 mm) and made air-tight with a rubber seal. The battery tester was an Interface 1000TM Potentiostat/Galvanostat/ZRA (Gamry Instruments, Inc.) electrochemical workstation with “Gamry Echem Analyst” software. The Raman data of charge-discharge cycles were analyzed (spectral deconvolution) using Lorentzian line shape functions in a home-built Matlab script. The chemical state of the sample surfaces was analyzed by X-ray photoelectron spectroscopy (XPS) measurements on a Specs XPS system with a Phoibos 150 energy analyzer. The spectra were recorded using monochromatized Al Kα radiation (400 W, 15 kV) at a detection angle of 45° with pass energies of 90 and 30 eV for survey and detail measurements, respectively. All binding energies were calibrated to the main C1s peak of C-C/C-H species at 284.8 eV. The peak fit was done with CasaXPS, using Shirley-type backgrounds and Gaussian-Lorentzian peak shapes.

**Simulations:** The conformation of the electrode materials in charged and discharged states was modeled via multiscale simulations. Various electrode and reagent configurations were initially calculated in classical UFF force fields using Monte Carlo algorithm to select the lowest energy geometries. Further geometry optimizations of all reagents and products in the gas-phase were performed at the density functional theory (DFT) level using hybrid B3LYP<sup>[3]</sup> functional with def2-TZVP basis set<sup>[4]</sup> and Grimme's D3-dispersion correction with Becke-Johnson damping, i.e., D3(BJ).<sup>[5]</sup> Geometry optimization was performed using Gaussian16 Rev. C. 01<sup>[6]</sup> with default ultra-fine grid for numerical integration and an energy convergence criterion of 10<sup>-8</sup> Hartree. All optimized geometries obtained were confirmed with vibrational analysis. Electrostatic potential maps (ESP) of PTPAn molecules and the formed coordination complex during the charge storage process were obtained using Gaussview 6.1.1.<sup>[7]</sup>

The Gibbs free energy of the formation reaction of the PTPAn<sup>n+</sup>-[B(hfip)<sub>4</sub>]<sup>-</sup> coordination complex and the redox potential in terms of single electron transfer were obtained using B3LYP-D3(BJ)/def2-TZVP via thermodynamic analysis implemented in Gaussian16 (at 298 K and 1 atm) according to the following equations:

$$\Delta G = \sum(G_{\text{products}} - G_{\text{reagents}}) \quad (3)$$

$$V = \frac{-\Delta G}{ne} \quad (4)$$

At equilibrium and constant pressure and temperature, the open-circuit cell voltage,  $V_{\text{cell}}$  is linked to the reaction Gibbs energy of the overall process  $\Delta_r G_{T,p}$  and was computed employing the Nernst equation:<sup>[35]</sup>

$$-nFV_{\text{cell}} = \Delta_r G_{T,p} = (\mu_{A_n\text{Host}} - \mu_{\text{Host}} - \mu_{A\oplus\ominus}) + \left( \mu_{A\oplus\ominus} - n\mu_{A_{(\text{gas})}^0} + n \left( \mu_{A_{(\text{gas})}^0} - n\mu_{A_{(\text{sol})}^0} \right) \right) \quad (5)$$

where  $\mu_i$  are the chemical potentials of the bulk and gas phases and  $\mu_{A_{(\text{sol})}^0}$  represents the chemical potential of the counter electrode (metallic alkali).

## SUPPORTING INFORMATION

*Electrochemical measurements:* The PTGNP cathodes were prepared by mixing the PTGNP composite with polytetrafluoroethylene (PTFE) binder in ethanol at a mass ratio of 9: 1 and dried at 85 °C for 12 h under vacuum. The mixture was then hot pressed (80°C) forming a free-standing film with a mass loading of 2 to 2.5 mg cm<sup>-2</sup> in an argon-filled glove box (H<sub>2</sub>O, O<sub>2</sub> <0.1 ppm). The CaSn<sub>3</sub>-alloy anode was prepared according to previously reported procedures.<sup>[12c]</sup> All electrochemical measurements were conducted with coin cells (CR2032), except for the three-electrode cyclic voltammetry (CV) test for which a PAT-Cell configuration (EL-Cell) was used. Each tested coin cell was comprised of a polished Mg-foil anode (Ca-pellet or CaSn<sub>3</sub>-alloy pellet anode), a PTGNP cathode with aluminum mesh as current collector, and two layers Whatman GF/C separators. 0.5 M Mg[B(hfip)<sub>4</sub>]<sub>2</sub>/DME and 0.25 M Ca[B(hfip)<sub>4</sub>]<sub>2</sub>/DME solutions were used as the electrolytes for Mg and Ca-ion systems, respectively, unless otherwise indicated. CV tests were carried out using a VMP3 potentiostat (Bio-Logic), while galvanostatic cycling and GITT measurements were conducted with an Arbin battery tester at 25 °C

## Supplementary Data

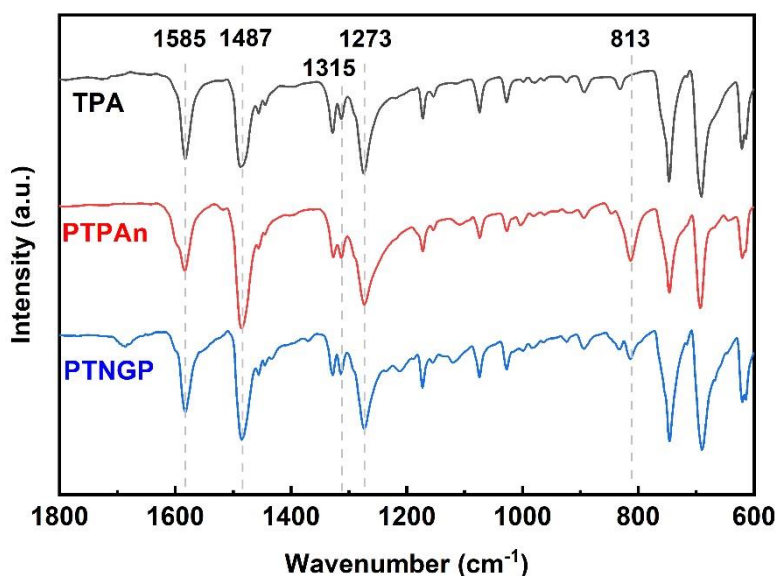


**Figure S1.** FT-IR spectra of the TPA monomer, the as-prepared PTPAn and PTGNP.

## SUPPORTING INFORMATION

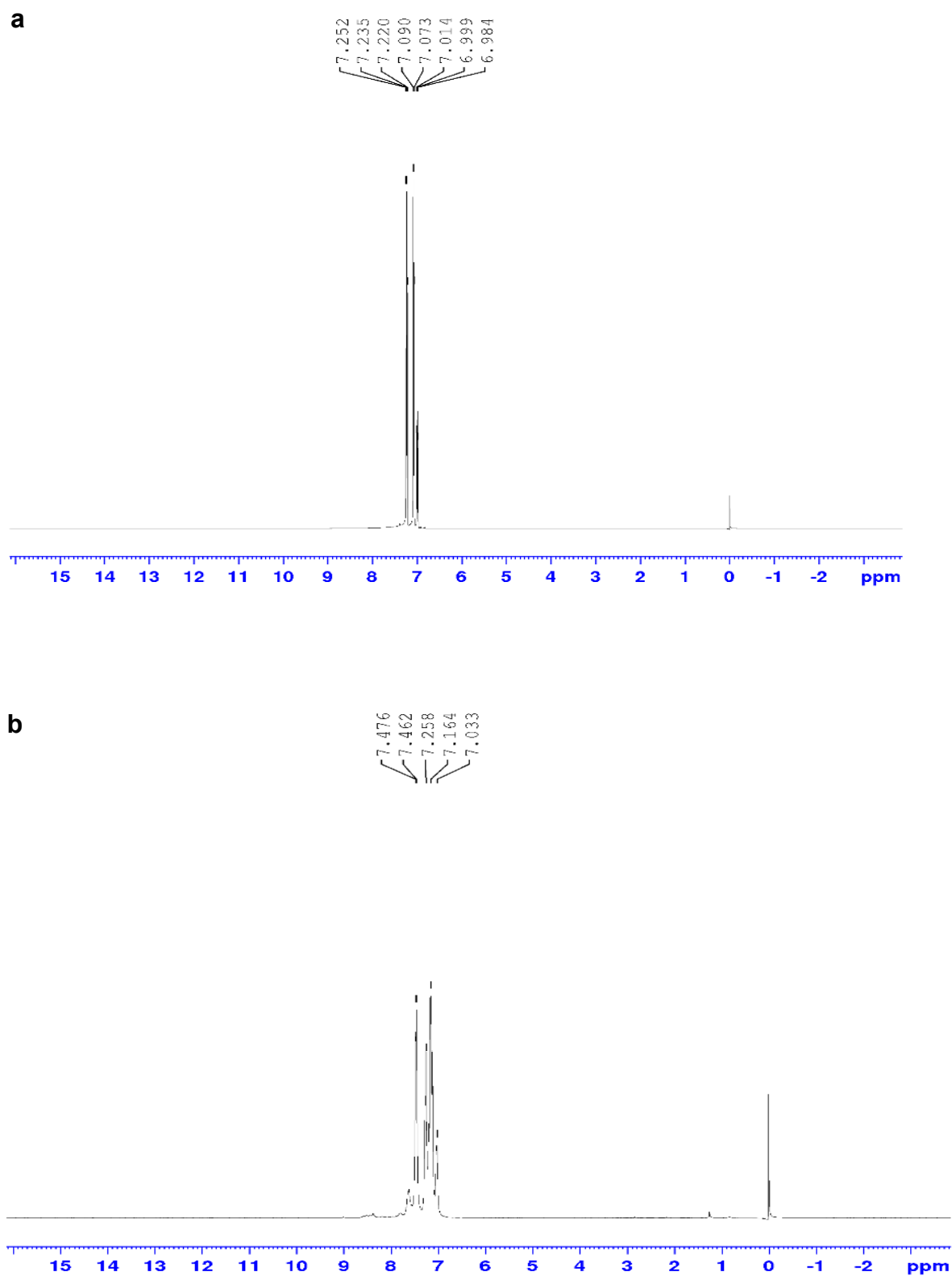


**Figure S2.**  $^1\text{H}$  NMR spectra (a) the monomer TPA and (b) PTPAn in  $\text{CDCl}_3$  solvent.

## SUPPORTING INFORMATION

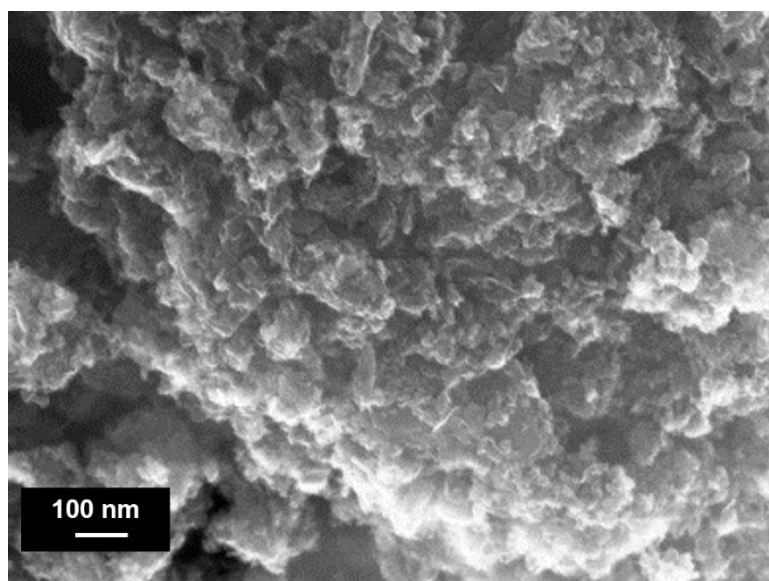


**Figure S3.** SEM image of as-prepared PTGNP composite.

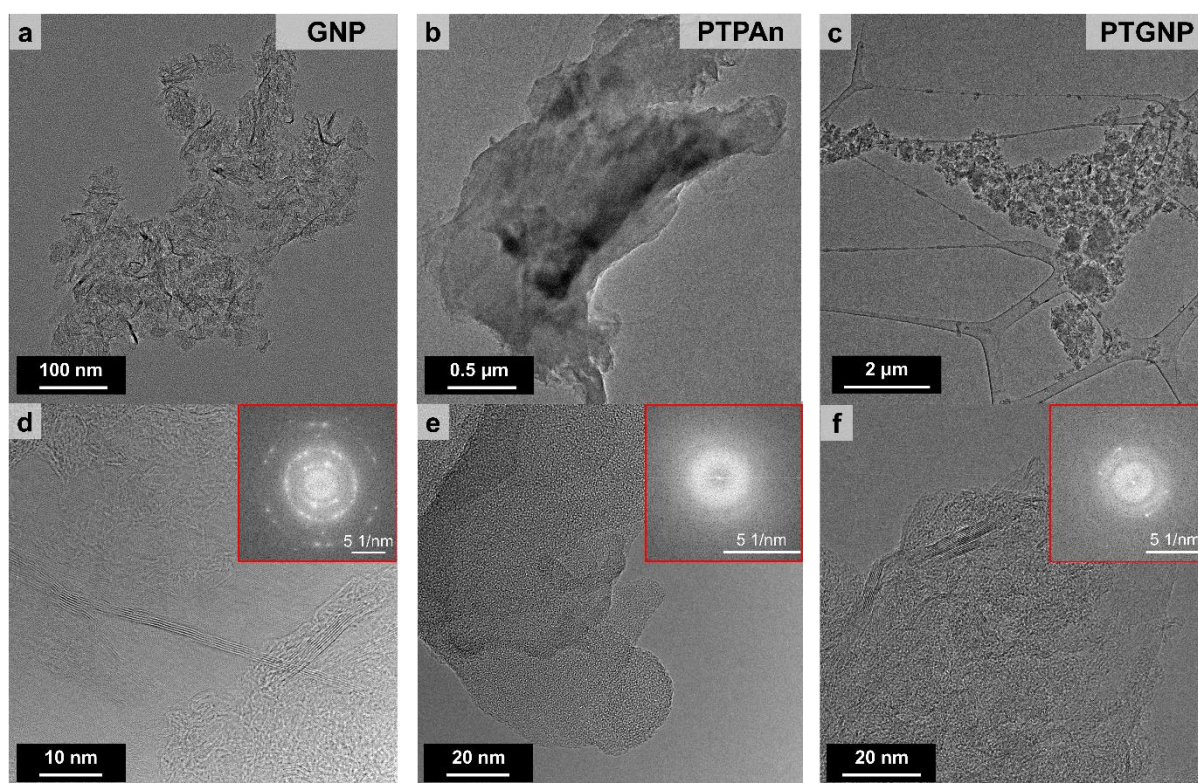


**Figure S4.** TEM and HRTEM images: (a, d) pristine GNP; (b, e) synthesized PTPAn polymer; and (c, f) as-prepared PTGNP composite (insets show the FFT patterns extracted from HRTEM images).

## SUPPORTING INFORMATION

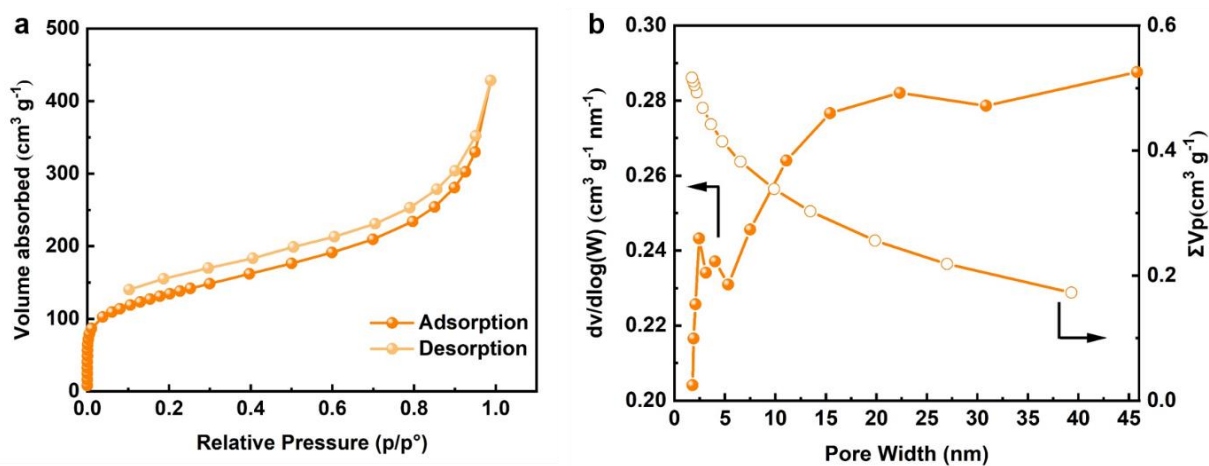


**Figure S5.** (a) Nitrogen adsorption/desorption isotherms of PTNGP composite, (b) Differential pore size distribution ( $dV_p/d\log(W)$ ) and cumulative pore volume ( $\Sigma V_p$ ) curves by Barrett-Joiner-Halenda-model analysis (BJH).

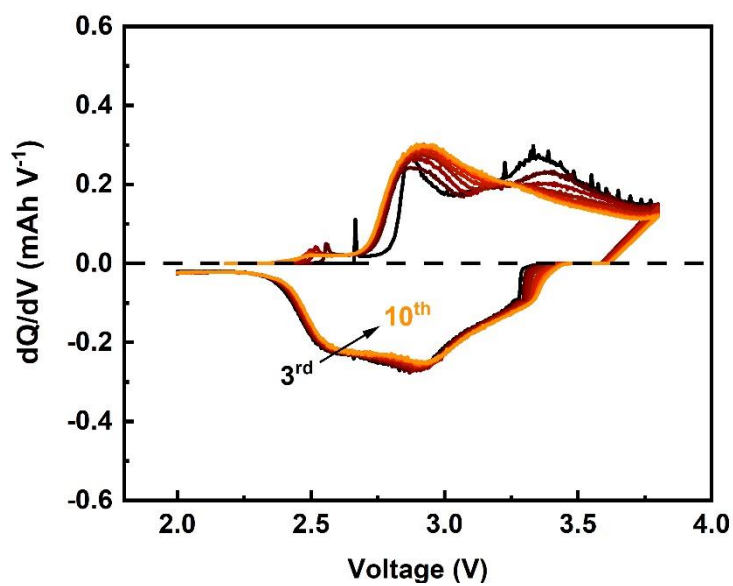


**Figure S6.** Differential capacity analysis of the Mg||PTNGP cell at 5C ( $1C = 109 \text{ mA g}^{-1}$ ).

## SUPPORTING INFORMATION

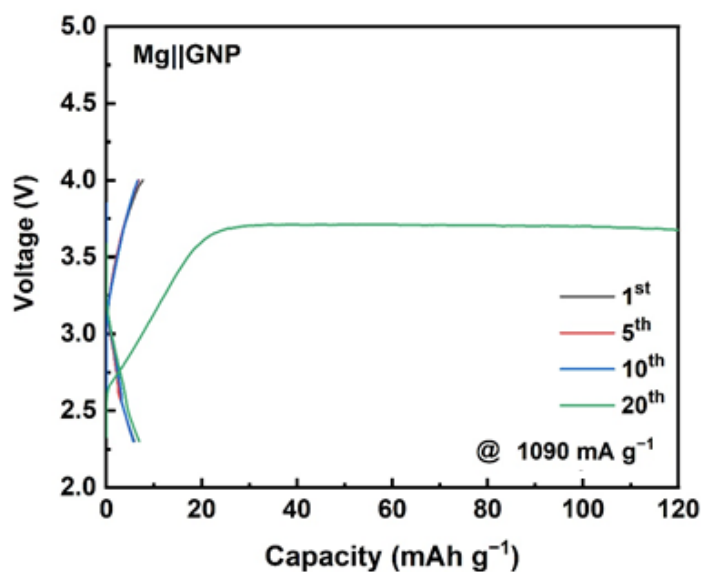


**Figure S7.** Galvanostatic charge/discharge voltage profiles of the GNP/PTFE electrode (GNP:PTFE = 9 : 1 , mass ratio) at the current density of 1090 mA g<sup>-1</sup>.

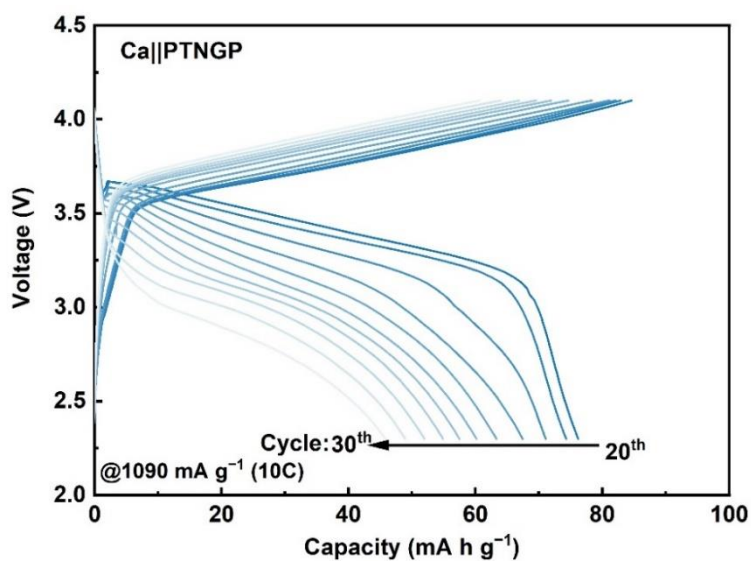


**Figure S8.** Galvanostatic charge/discharge voltage profiles of the Ca||PTNGP full cell at 10C (1C = 109 mA g<sup>-1</sup>).

## SUPPORTING INFORMATION

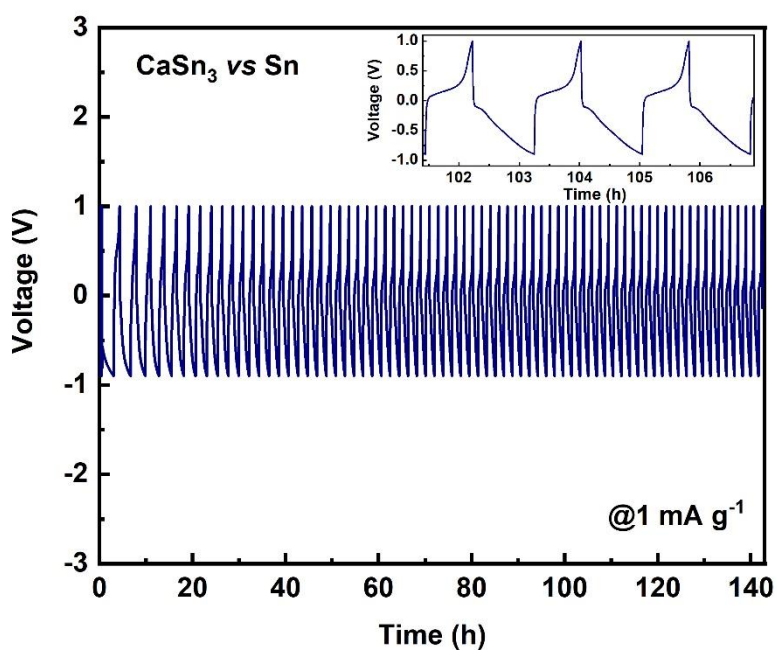


**Figure S9.** Galvanostatic voltage profiles of the half-cells comprising a  $\text{CaSn}_3$  alloy anode and a Sn counter electrode at a current density of  $1 \text{ mA g}^{-1}$ .

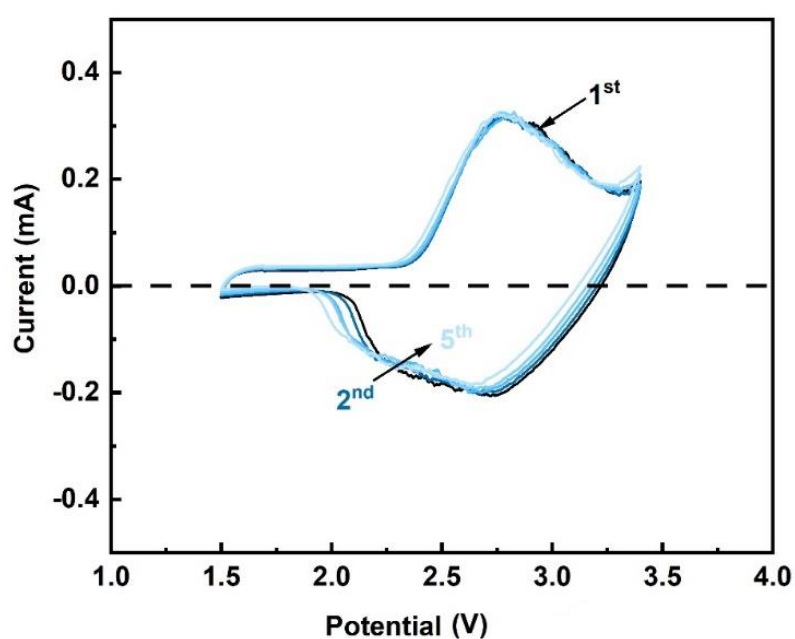


**Figure S10.** CVs of the PTGNP cathode using  $\text{CaSn}_3$  as both counter and reference electrodes at a scan rate of  $1 \text{ mV s}^{-1}$ .



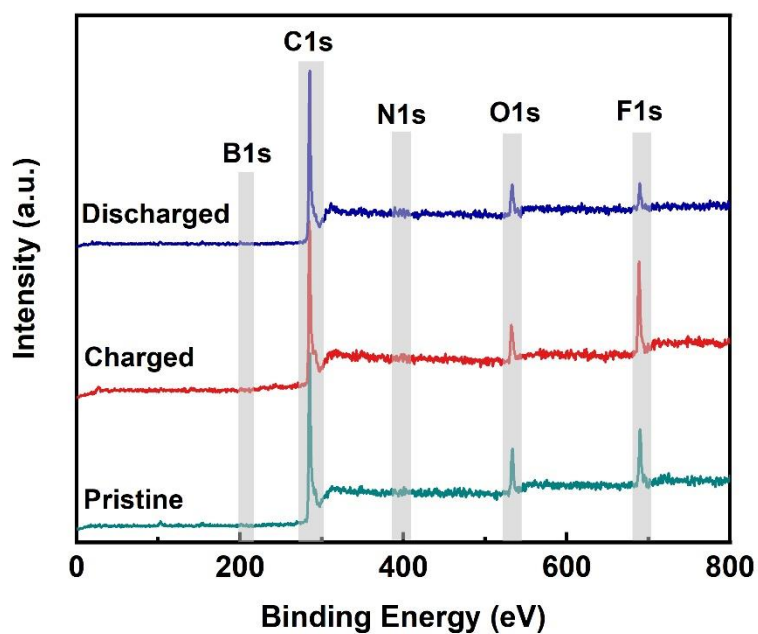


**Figure S11.** XPS survey spectra of PTGNP cathodes at different charge states.

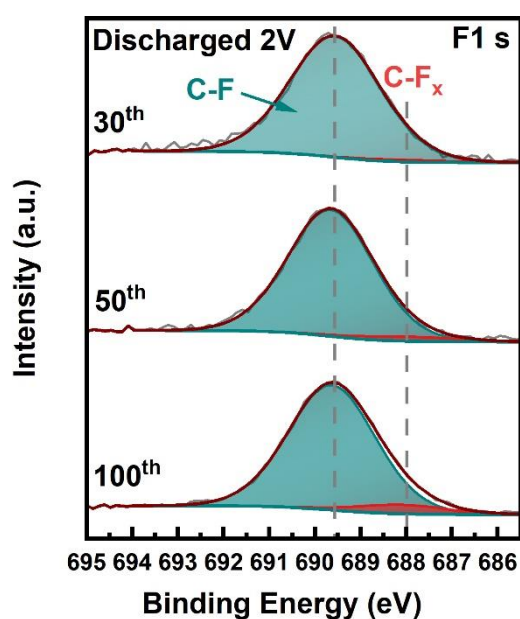


**Figure S12.** High-resolution XPS spectra in F1 s region of fully discharged PTGNP cathodes in the 30<sup>th</sup>, 50<sup>th</sup> and 100<sup>th</sup> cycles, respectively.

**Table S1.** Quantitative analysis of the F1 s region in high-resolution XPS spectra for fully discharged PTGNP cathodes in the 30<sup>th</sup>, 50<sup>th</sup> and 100<sup>th</sup> cycle, respectively.

	C-F	C-F <sub>x</sub>
30 <sup>th</sup> cycle	3.16%	0.05%
50 <sup>th</sup> cycle	5.23%	0.21%
100 <sup>th</sup> cycle	7.71%	0.56%

## SUPPORTING INFORMATION

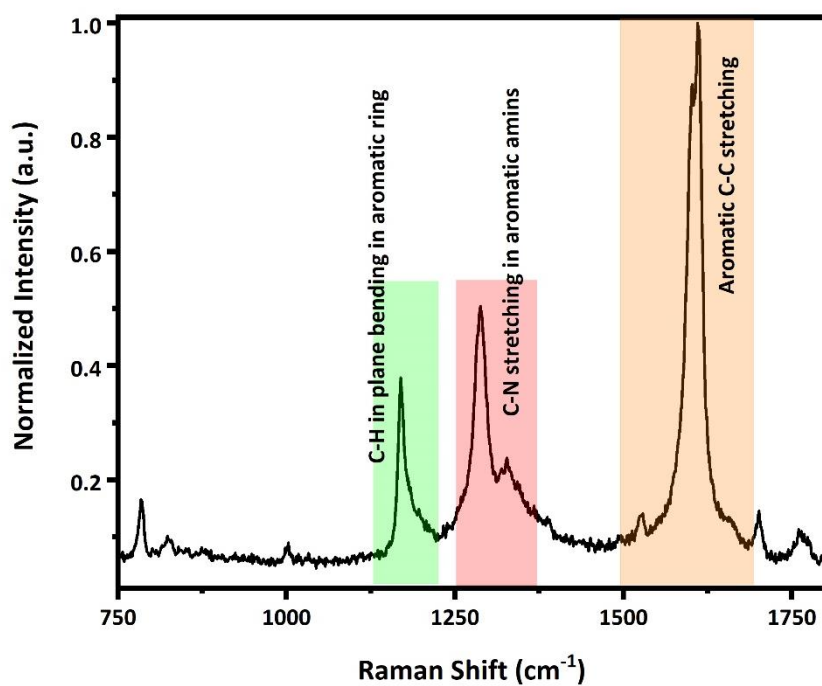


**Figure S13.** Ex-situ Raman spectrum of pristine PTPAn active material.

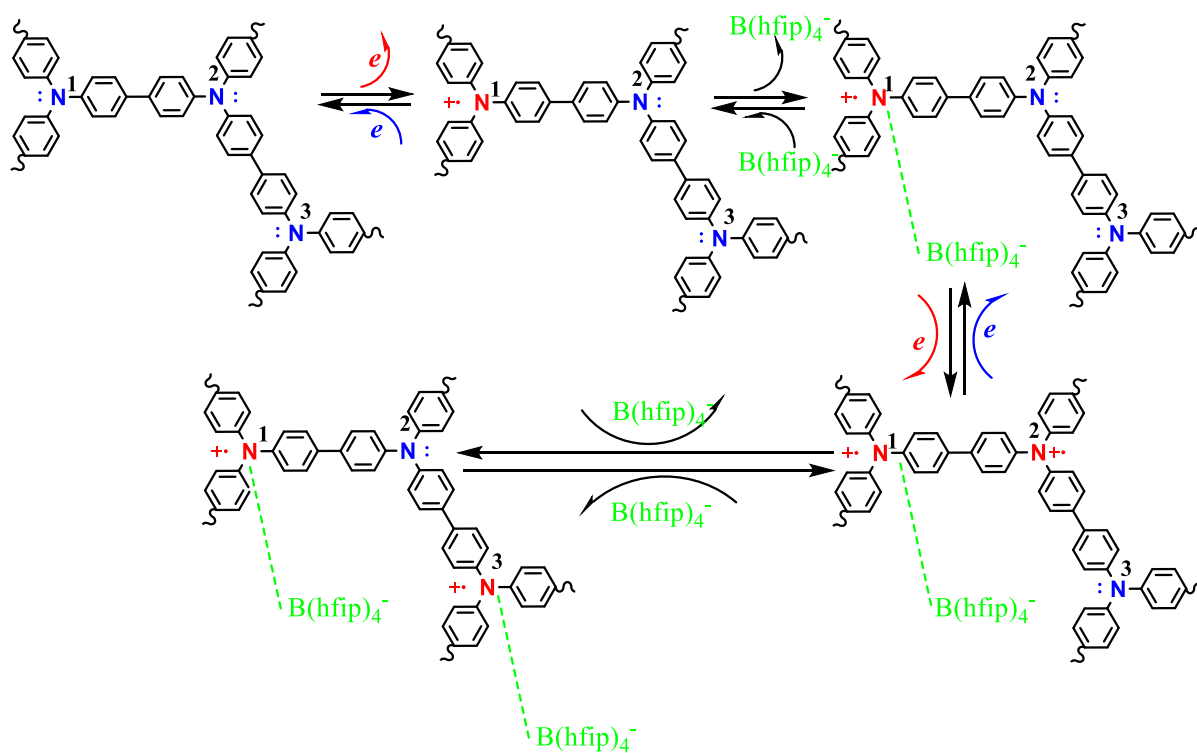


**Figure S14.** Scheme of structural evolution of PTPAn associated with electron-transfer during redox reactions.

## SUPPORTING INFORMATION

## References:

- [1] a) C. Takahashi, S. Moriya, N. Fugono, H. C. Lee, H. Sato, *Synth. Met.* **2002**, *129*, 123–128; b) J. K. Feng, Y. L. Cao, X. P. Ai, H. X. Yang, *J. Power Sources* **2008**, *177*, 199–204.
- [2] Z. Zhao-Karger, M. E. Gil Bardaji, O. Fuhr, M. Fichtner, *J. Mater. Chem. A* **2017**, *5*, 10815–10820.
- [3] Alex D. Beck, *J. Chem. Phys.* **1993**, *98*, 5648.
- [4] A. Schäfer, H. Horn, R. Ahlrichs, *J. Chem. Phys.* **1992**, *97*, 2571–2577.
- [5] S. Grimme, S. Ehrlich, L. Goerigk, *J. Comput. Chem.* **2011**, *32*, 1456–1465.
- [6] Gaussian 16, Revision C.01, M. J. Frisch, G. W. Trucks, H. B. Schlegel, G. E. Scuseria, M. A. Robb, J. R. Cheeseman, G. Scalmani, V. Barone, G. A. Petersson, H. Nakatsuji, X. Li, M. Caricato, A. V. Marenich, J. Bloino, B. G. Janesko, R. Gomperts, B. Mennucci, H. P. Hratchian, J. V. Ortiz, A. F. Izmaylov, J. L. Sonnenberg, D. Williams-Young, F. Ding, F. Lipparini, F. Egidi, J. Goings, B. Peng, A. Petrone, T. Henderson, D. Ranasinghe, V. G. Zakrzewski, J. Gao, N. Rega, G. Zheng, W. Liang, M. Hada, M. Ehara, K. Toyota, R. Fukuda, J. Hasegawa, M. Ishida, T. Nakajima, Y. Honda, O. Kitao, H. Nakai, T. Vreven, K. Throssell, J. A. Montgomery, Jr., J. E. Peralta, F. Ogliaro, M. J. Bearpark, J. J. Heyd, E. N. Brothers, K. N. Kudin, V. N. Staroverov, T. A. Keith, R. Kobayashi, J. Normand, K. Raghavachari, A. P. Rendell, J. C. Burant, S. S. Iyengar, J. Tomasi, M. Cossi, J. M. Millam, M. Klene, C. Adamo, R. Cammi, J. W. Ochterski, R. L. Martin, K. Morokuma, O. Farkas, J. B. Foresman, and D. J. Fox, Gaussian, Inc., Wallingford CT, **2016**.
- [7] GaussView, Version 6.1.1, Roy Dennington, Todd Keith, and John Millam, Semichem Inc., Shawnee Mission, KS, **2019**.